Microfluid Nanofluid (2017) 21:82
DOI 10.1007/s10404-017-1917-4

RESEARCH PAPER

Micromixing with spark-generated cavitation bubbles

Salvatore Surdo[1] · **Alberto Diaspro**[1] · **Martí Duocastella**[1]

Received: 21 November 2016 / Accepted: 6 April 2017 / Published online: 13 April 2017
© Springer-Verlag Berlin Heidelberg 2017

Abstract The intrinsic laminarity of microfluidic devices impedes the mixing of multiple fluids over short temporal or spatial scales. Despite the existence of several mixers capable of stirring and stretching the flows to promote mixing, most approaches sacrifice temporal or spatial control, portability, or flexibility in terms of operating flow rates. Here, we report a novel method for rapid micromixing based on the generation of cavitation bubbles. By using a portable battery-powered electric circuit, we induce a localized electric spark between two tip electrodes perpendicular to the flow channel that results in several cavitation events. As a result, a vigorous stirring mechanism is induced. We investigate the spatiotemporal dynamics of the spark-generated cavitation bubbles and quantify the created flow disturbance. We demonstrate rapid (in the millisecond timescale) and efficient micromixing (up to 98%) within a length scale of only 200 μm and over a flow rate ranging from 5 to 40 μL/min.

Keywords Active mixer · Cavitation bubbles · Rapid mixing · Pocket microfluidics · Portable sensors

1 Introduction

Rapid mixing of two or more liquids at the microscale (micromixing) is an essential step for the control of chemical reactions in microfluidic devices, including lab-on-chip (LoC), micro total analysis systems (μ-TAS), and microreactors for chemical synthesis (Dittrich et al. 2006; Chan et al. 2010; Jeong et al. 2010; Elvira et al. 2013; Singh et al. 2016). However, mixing fluids in microchannels (diameter below 1 mm) constitutes one of the classical problems of microfluidics. Indeed, at this scale viscosity dominates over inertia (low Reynolds number) and flows are laminar and uniaxial. Thus, mixing two parallel streams will only occur from the molecular diffusion through the liquid interface. Because diffusion is slow compared to the advective transport of mass along the flow direction, the resulting mixing length can be prohibitively long. The dimensionless Péclet number (*Pe*), namely the ratio between advection and diffusion, provides an estimation of the length L_{mix} that is required to complete mixing by purely diffusive mechanisms (Stroock et al. 2002; Suh and Kang 2010; Nguyen 2012). For instance for a microchannel with a width $l = 100$ μm, a mean flow velocity $U = 1$ mm/s, and a molecular diffusivity $D = 10^{-10}$ m^2/s, the resulting mixing length $L_{mix} \sim Pe \cdot l$, where $Pe = Ul/D$, is about 10 cm. This clearly defies the core concept of miniaturization and portability of microfluidic-based systems.

A myriad of approaches have been developed to enhance micromixing (Suh and Kang 2010; Lee et al. 2011). Regardless of their specific design and implementation, the fundamental strategy has been to reduce the distance between unmixed fluids so as to decrease the diffusion length, i.e., the length necessary to homogenize the fluid considering a purely diffusive process. Hence, the main

Electronic supplementary material The online version of this article (doi:10.1007/s10404-017-1917-4) contains supplementary material, which is available to authorized users.

✉ Martí Duocastella
marti.duocastella@iit.it

[1] Nanophysics Department, Istituto Italiano di Tecnologia, Via Morego 30, 16163 Genoa, Italy

difference between existing methods lies in how to apply this strategy. In general, one can distinguish two broad groups: passive mixers and active mixers.

Passive mixers use engineered microfluidic systems with a specially designed architecture to favor mixing. They include parallel lamination mixers, based on the splitting and recombination of the flow streams by microchannels with complex geometry, or chaotic advection mixers, in which the flowing streams are repeatedly stretch and fold using serpentine channels or obstacles transverse to the flow (Stroock et al. 2002; Therriault et al. 2003; Schönfeld et al. 2004; Buchegger et al. 2011). Whereas the use of parallel lamination can induce efficient and rapid mixing, the complexity of the associated fabrication processes, with typical channels diameters of few μm, constraints its implementation in advanced microfluidic devices. In contrast, mixers based on chaotic advection can be fabricated with simple and inexpensive technologies such as soft lithography. These mixers, though, require a high flow velocity to induce rapid mixing (Stroock et al. 2002), which may be difficult to attain in certain instances. For practical applications, efficient mixing is highly desirable over a wide range of flow rates (Jeong et al. 2010). More importantly, all passive mixers lack an on/off switching mechanism of the mixing process—the process starts upon fluids entering the mixing chamber. Therefore, the degree of temporal and spatial control achievable with these mixers is inherently limited.

Active mixers use an external energy source, e.g., thermal (Sigurdson et al. 2005), electric (Chen and Cho 2008; Song et al. 2010), magnetic (Wen et al. 2009; Ballard et al. 2016), and acoustic (Yaralioglu et al. 2004; Ahmed et al. 2009; Luong et al. 2010), to induce a transverse disturbance in the flow capable of stretching and folding the fluids and hence promote rapid mixing. Compared to passive mixers, the control of the external source enables to switch on/off the mixing process. Moreover, active mixers can typically operate over a wide range of flow velocities (i.e., flow rates). Unfortunately, their performance is significantly affected by the magnitude and frequency of the transverse disturbance. As a rule of thumb, to achieve good mixing a strong transverse disturbance driven at a high frequency (with respect to the flow rate) is needed. This can be challenging to achieve, at least without sacrificing some of the fundamental premises of microfluidic systems. For instance, by means of acoustic/ultrasonic actuation, strong streams can be induced at high operational frequencies, up to 450 MHz (Yaralioglu et al. 2004). This produces efficient mixing over different flow rates, but it comes at the cost of external bulky and expensive instrumentation (e.g., tunable AC generator) that defies device portability. In contrast, current systems that offer high portability fail to accomplish the generation of strong disturbances. For example, electroosmotic mixers based on electrokinetic instabilities enable efficient mixing (>90%) by using small AC driving signals (e.g., 5 V peak to peak) and a low operational frequency (~1 Hz) (Sasaki et al. 2006; Song et al. 2010). However, the low magnitude of the induced transverse velocity (~100 μm/s) compared with the typical velocities of the driving flow (>1 mm/s) must be compensated by the use of a long residence time, namely fluids must be subjected to prolonged interactions with the external disturbance. Consequently, most electroosmotic mixers are only operational at low flow rates, which greatly limits the mixing throughput (<μL/min), and/or require long mixing chambers (~mm), which reduces control and selectivity of the chemical reactions and minimum volume of mixed fluid.

A promising strategy to induce close-to-ideal fluid actuation is the generation of cavitation bubbles (Brennen 1995; Zwaan et al. 2007). The rapid collapsing of a cavitation bubble in proximity to a solid boundary (e.g., the channel walls) generates jetting and vortices that stir the fluid at high velocities (Zwaan et al. 2007; Duocastella et al. 2009). Indeed, jet velocities up to 10^4 mm/s and vortices with initial rotation rate of 10^4 s^{-1} have been demonstrated for a single bubble collapsing near a single solid boundary (Zwaan et al. 2007). Despite the unique features in the magnitude and speed of the transverse disturbance generated, not until recently has cavitation been used in microfluidic applications such as microdroplets generation (Park et al. 2011; Duocastella et al. 2015) and micropumping (Dijkink and Ohl 2008). To our knowledge, only two works have been published regarding micromixing by cavitation (Hellman et al. 2007; Ozcelik et al. 2014). The first is based on laser-induced cavitation, namely the formation of a cavitation bubble in a microchannel by optical breakdown in the liquid. This resulted in efficient mixing of a small volume of fluid (0.5–1.5 nL) flowing at ~1.67 μL/min and 7 mm downstream from the cavitation site (Hellman et al. 2007). The second study involves the combination of acoustic waves with a microchannel with wavy walls to facilitate cavitation bubble growth, which allowed mixing of highly viscous fluids (~50 mPa s) (Ozcelik et al. 2014). The implementation of cavitation-based mixing, though, has been seriously limited by the cost and size of the external instrumentation required to induce bubble formation (e.g., high-power laser). Not only is this equipment difficult to find in analysis or chemistry laboratories, but its intrinsic incompatibility with portable systems has prevented the widespread use of this mixing strategy.

Here, we present a novel method for micromixing via cavitation that addresses the major problems of current systems. Our approach consists of using a localized electric spark to induce electrical breakdown of a fluid and consequent cavitation bubble generation (Fig. 1a).

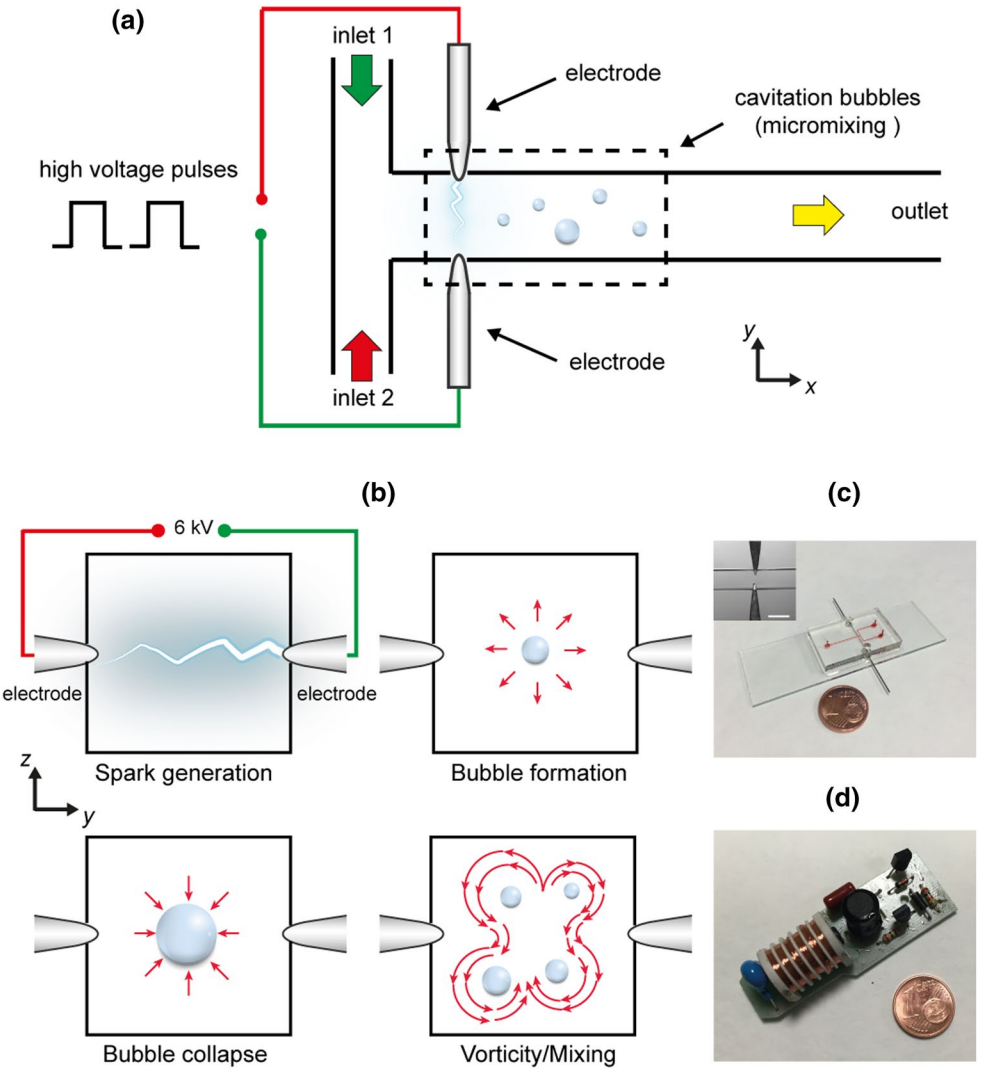

Fig. 1 Operating principle and implementation of our mixer. **a** Schematic representation (not in scale) of the micromixing device. **b** The application of a high-voltage pulse between two tip electrodes results in an electric spark and in the subsequent formation of a cavitation bubble. The bubble collapse generates smaller bubbles and vortices that perturb the fluid. **c** Optical image of the microfluidic chip filled with *red-dyed water* for highlighting the T-channel geometries. The *inset* shows two tip electrodes placed perpendicular to the main channel. *Scale bar* 200 μm. **d** Optical image of the portable electric circuit used as spark generator (color figure online)

Notably, this strategy offers a unique feature that existing cavitation methods lack, namely the possibility to generate the cavitation events using a simple, low-cost, and portable electronic circuit. In this work, we used a user-designed portable circuit capable of generating 6 kV pulses from a 1.5 V battery to investigate, for the first time, micromixing by spark-generated cavitation bubbles. We assessed the transverse disturbance to the flow induced by the dynamics—formation, expansion, and collapse—of the generated bubbles, and quantified the resulting mixing performance in terms of degree of mixing and mixing time. We also evaluated the effects of several technological parameters, including spark repetition rate and flow velocity, on the mixing process achievable with our pocket-size device.

2 Experimental

Micromixers based on spark-induced cavitation consist of a standard microfluidic T-channel (230 μm wide) with two tip electrodes placed perpendicular to the main channel. The T-channel was fabricated in polydimethylsiloxane (PDMS) using single-step soft lithography (Qin et al. 2010). More in detail, photolithography was used to first pattern a master into a layer of 260-μm-thick SU-8-100 photoresist applied on top of a 4-in. silicon wafer by spin coating. Once the photoresist master was ready, the PDMS prepolymer was poured onto the master with a cross-linker (mass ratio 10:1), degassed in a vacuum for 30 min, and cured at 60 °C for 1 h. After curing, the PDMS pattern was peeled off from the master, and inlet and outlet holes were

perforated using a punch with diameter of 1.0 mm (Unicore, Ted Pella). The microfluidic chip was sealed to a microscope glass by O_2 plasma bonding (RF power 60 W, exposure time 20 s).

Two electrodes in tip-to-tip configuration were integrated into the microfluidic chip by simply punching the PDMS with two stainless steel pins (diameter of 200 μm and tip radius ~50 μm) (Fig. 1c). Note that the use of punched electrodes avoids complicated microfabrication processes and enables integration of the mixer into microfluidic devices with minimal additional costs. We did not observe damage of the electrodes during the entire study performed in this manuscript. However, for electrodes with lower radius of curvature, some erosion of the tip was visible after several discharge events.

A portable user-designed electronic circuit inspired by a commercial gas lighter (Fig. 1c) was used as spark generator. This circuit generates short (in the μs timescale) high-voltage pulses (up to 9 kV) using a common 1.5 V rechargeable battery. To enable the generation of a single spark, the standard mechanical switch of the gas lighter was replaced with a bipolar transistor that switches on/off the circuit through the use of a low-power signal (e.g., a TTL signal). To control the spark repetition rate from 16 to 160 Hz, the bias voltage was tuned from 1.2 to 3 V. This low-voltage control is compatible with the output signal of a cell phone. To optimize the conditions for cavitation-induced mixing, we tested three different voltage peak amplitudes. We observed that at 3 kV, no cavitation bubbles were generated. At 6 kV, cavitation bubbles were formed that resulted in good mixing. As the peak voltage amplitude was further increased to 9 kV, the generated cavitation bubbles were so large that they caused clogging of the microchannel. Therefore, to induce cavitation without compromising the functionalities of the mixer, throughout the manuscript we used voltage pulses of 6 kV. A schematic description of the final circuit is shown in Fig. S1 (Supplementary).

The fluid used in all the experiments was water with the addition of ~5×10^{-3} mol/dm^3 of phosphate-buffered saline (PBS). Because of the low concentration of PBS, our solution can be considered to have the same fluid dynamic properties of water, namely density of 0.998 g/cm^3 and viscosity of 1.002 mPa s (Hai-lang and Shi-jun 1996).

Time-resolved images of spark-generated cavitation bubbles were acquired using a stroboscopic imaging system. A single high-voltage pulse was used to induce the cavitation bubble. Images were captured with a sCMOS camera (Zeyla, Andor) mounted on an inverted microscope (Nikon, Eclipse Ti-E with Objective 10X-0.45NA) by flashing a high-power white LED for 500 ns. The synchronization signal to trigger the LED flash was provided by the high-voltage pulse at the output of the spark generation circuit, directly measured using a high-voltage probe (HVP40, SRS Electronics). A pulse delay generator (SG 535, Stanford Research Systems) was used to set the delay between the spark and the LED flash. The jitter between the triggering signal and the LED was preliminary characterized using a photodiode (DET10A, Thorlabs) and an oscilloscope (Wave Jet, LeCroy). The jitter was below 500 ns, thus leading to a total temporal resolution of ~1 μs. To ensure good reproducibility, several images (up to 30) were acquired for each delay time.

Particle image velocimetry (PIV) was used to characterize the flow after bubble collapse using a high-speed sCMOS camera (Zeyla, Andor) operating at 566 FPS. Fluorescent microbeads (Invitrogen, 1 μm in size, $\lambda_{ex} = 580$ nm, $\lambda_{em} = 605$ nm) diluted in PBS:H_2O (~5×10^{-3} mol/dm^3, 1 mS/cm) were used as flow tracers. The channel was illuminated from the top using a high-pressure mercury lamp and the microbeads motion was recorded from the bottom (transmission). A TRITC filter ($\lambda_{cutoff} = 595$ nm) was used to cut off the excitation light and to capture the emission light from the beads. The velocity field was evaluated by cross-correlation methods using the PIV plugin of ImageJ (Schindelin et al. 2012). The method was applied on a region of 155 × 310 pixels using a 16 × 16 pixel (~5 μm × 5 μm) interrogation window with 50% overlapping between adjacent windows.

High-speed fluorescence microscopy was used for visualizing the mixing process. The fluorescent dye was fluorescein ($\lambda_{ex} = 490$ nm; $\lambda_{em} = 514$ nm, Sigma-Aldrich), dissolved in deionized water (DI-H_2O) at a concentration of 2×10^{-5} mol/dm^3. This fluorescent solution was introduced into the T-channel of the microfluidic circuit using a syringe pump (Nexus 6000, Chemyx) that operated in withdraw mode. Thus, flow rates from 5 to 40 μL/min with mean flow velocities from 1.3 to 10.7 mm/s could be generated. The conductivity of both solutions was adjusted to 1 mS/cm using ~5×10^{-3} mol/dm^3 of PBS with pH 7.2. The mixing performances were evaluated through dilution experiments by recording the dye intensity during the mixing. Time-resolved fluorescence images with resolution of 2036 × 336 pixel were recorded at 500 FPS using the same setup used for the PIV experiments. A FITC filter ($\lambda_{cutoff} = 505$ nm) was used to cut off excitation light and to capture the emission light from the dyes. A pulse generator (SG 535, Stanford Research Systems) and a power supply (E3612A, Agilent) were used to bias the electronic circuit and control the spark repetition rate from 16 to 160 Hz.

3 Results and discussion

3.1 Spark-induced cavitation in the channel

Initially, we used time-resolved microscopy to demonstrate that our mixer was capable of cavitation bubble

generation. In particular, we characterized the dynamics of the fluid flowing between the electrodes (2.7 mm/s) after the application of a single high-voltage pulse. A representative example of the waveform of one of these pulses generated with our electric circuit is shown in Fig. 2a. The voltage pulse corresponds to a damped sine wave with an amplitude of 6 kV, a period of 25 μs, and a total duration of 200 μs. This particular waveform, caused by the parasitic resistance of the system, is key to understand the events shown in the time series of Fig. 2b. At $\Delta t = 0.0$ μs, the first electric discharge induces the generation of a visible plasma (spark) between the tip electrodes. As a result, a cavitation bubble is rapidly formed that nucleates at the upper positively polarized electrode ($\Delta t = 5.0$ μs). Note that the voltage required to induce dielectric breakdown in liquids is usually lower when the polarity of the tip electrode is positive than when it is negative (Qian et al. 2006). Therefore, when a symmetrical electrode configuration is used, the dielectric breakdown, and thus the cavitation bubble nucleation, preferentially initiates at the positively charged electrode (Bruggeman et al. 2009). After the nucleation step, the bubble starts growing toward the middle of the channel—expansion phase—and reaches its maximum size (i.e., 145 ± 8 μm in diameter) at $\Delta t = 35.0$ μs. At this point, a second bubble originates from the lower electrode. This correlates well with the existence of a negative peak (−3.1 kV at 35 μs) in the pulse waveform. After reaching its maximum size, the first bubble rapidly collapses ($\Delta t = 45$ μs) generating secondary smaller bubbles with a diameter of about 30 μm. At $\Delta t = 50$ μs, only secondary bubbles in the center of the microchannel can be observed. This instance, though, is followed by the formation of a third cavitation bubble from the upper electrode. As in the previous cases, this episode coincides with a voltage peak (with amplitude ~2.9 kV at $\Delta t = 60$ μs) of the driving pulse. After the final collapse of the third bubble at $\Delta t = 70$ μs, no additional events of relevance occur. Only the presence of some secondary bubbles with a diameter below 10 μm can be distinguished within the cavitation site up to $\Delta t \sim 10$ ms. This seems to indicate that, even if the rapid dynamics of the multiple cavitation bubbles are in the microsecond timescale, the flow is still disturbed milliseconds after the application of the high-voltage pulse. As detailed next, further experiments were carried out to shed light on this point.

3.2 Transverse velocity and vorticity generation

To quantify the magnitude and temporal scale of the vorticity and stirring flows induced by the cavitation process, we studied the flow velocity field using microparticle image velocimetry (Supplementary Fig. S2). Figure 3a, b shows the longitudinal (U_X) and transverse (U_Y) components of the velocity field before cavitation bubble formation as well as after bubble collapse. Under steady-state conditions ($\Delta t = 0.0$ s), the flow is uniaxial (laminar) and the velocity field features a parabolic cross-sectional profile as expected for a pressure-driven, i.e., Hagen–Poiseuille, flow. In particular, we found a maximum flow velocity $U_X \sim 1.55$ mm/s in agreement with the imposed flow rate, and a negligible transverse flow, $U_Y \sim 0$ mm/s. In contrast, after the collapse of the spark-generated cavitation bubbles

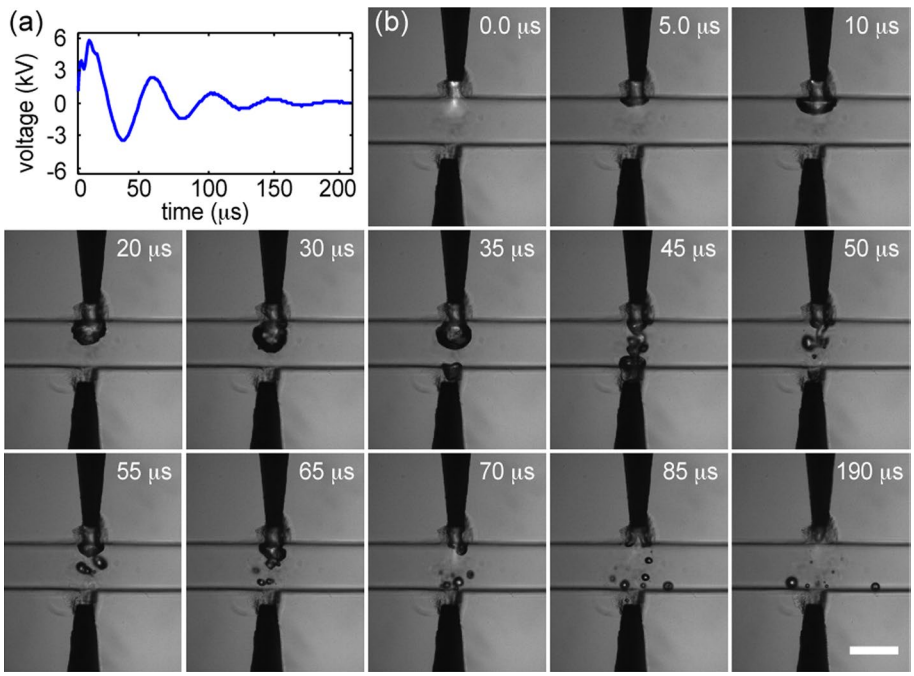

Fig. 2 Bubble dynamics characterized by time-resolved imaging. **a** A typical voltage pulse generated with the electric circuit. The pulse is a damped sine wave with amplitude of 6 kV, time period of ~25 μs, and decay time of ~200 μs. **b** Series of time-resolved images showing the dynamics—formation, expansion, and collapse—of a cavitation bubble generated using a single high-voltage pulse like the one in (**a**). The flow is from *left* to *right*, and the *bar* indicates a length of 200 μm

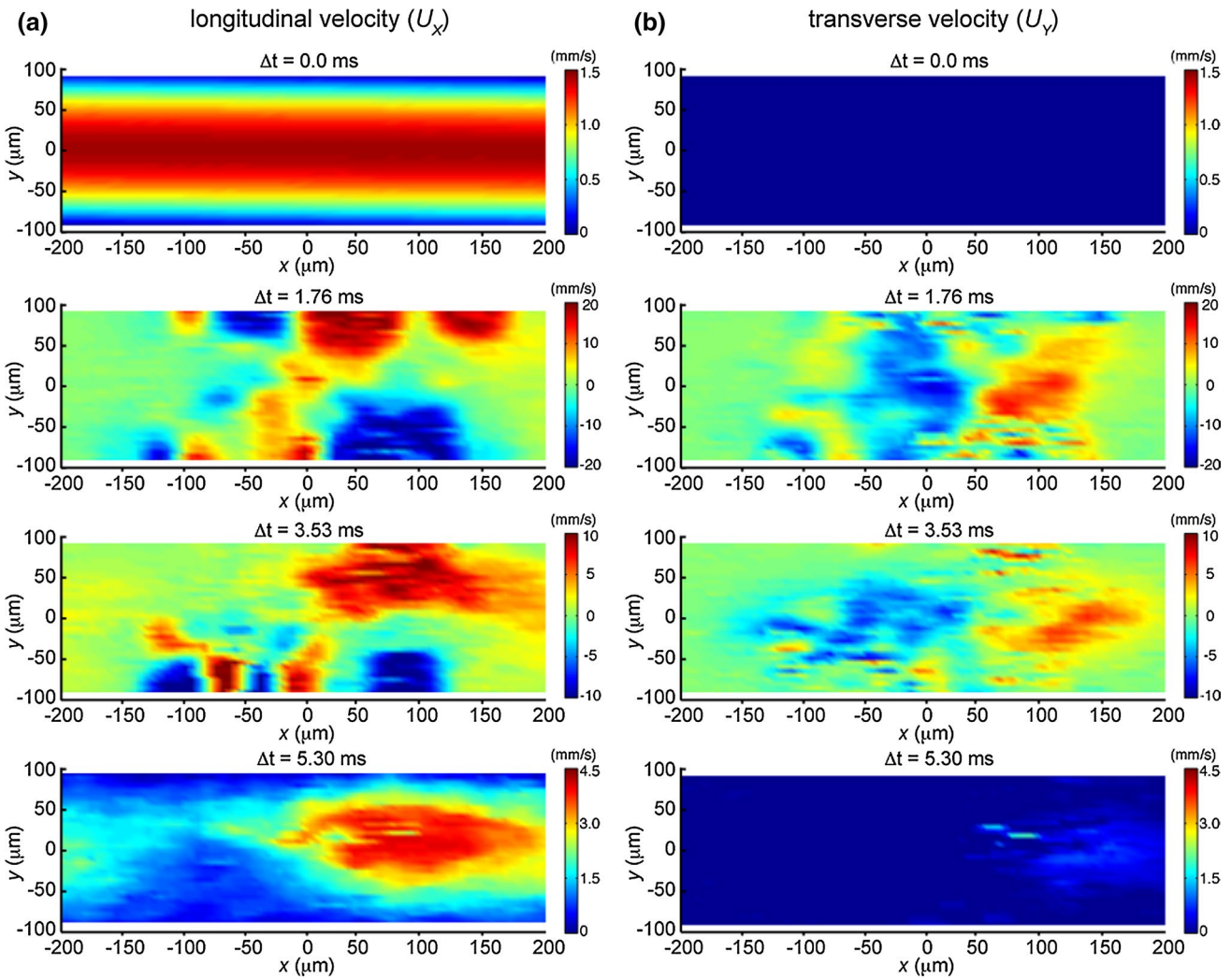

Fig. 3 Microparticle image velocimetry. **a** Time evolution of the longitudinal (**a**) and transverse (**b**) components of the velocity field before and after bubble collapse. **b** The flow is from *left* to *right*, and the coordinate $X = 0$ denotes the position of the tip electrodes

($\Delta t = 1.76$ ms), a transverse flow is generated with a maximum velocity $U_Y \sim 15$ mm/s. Notably, this velocity is one order of magnitude higher than the imposed flow velocity. As the time progresses ($\Delta t = 3.53$ ms), the velocity field evolves in a clockwise rotating vortex with a maximum transverse velocity $U_Y \sim 8.8$ mm/s that progressively vanishes until reaching $U_Y \sim 0$ mm/s at $\Delta t = 5.30$ ms. After that, at $\Delta t \sim 10$ ms (not shown in Fig. 3), the stirred fluid flows downstream and the initial uniaxial Hagen–Poiseuille flow is completely restored.

A deeper insight into the recirculation of fluids can be obtained by calculating the vorticity of the velocity field, namely $\omega = \nabla \times u$ (Fig. 4). After bubble collapse ($\Delta t = 1.76$ ms), the vorticity map reveals the chaotic nature of the induced flow, with two distinct features clearly discernible: upstream of the electrodes ($x < 0$), the vorticity is mainly negative (i.e., counterclockwise rotations), while downstream ($x > 0$) the vorticity is mainly positive (i.e., clockwise rotations). Importantly, portions of the fluid achieve high rotation speeds, above 1000 s^{-1}. This high value demonstrates the power of the cavitation-induced stirring process. At $\Delta t = 3.53$ ms, the negative vorticity tends to vanish and the fluid prevalently rotates clockwise with a maximum rate of about 700 s^{-1}. Finally, at $\Delta t = 5.30$ ms, all velocity vectors are basically aligned to the direction of the pressure-driven flow and the vorticity vanishes within the analyzed region.

3.3 Flow instability with spark-induced cavitation

The previous PIV analysis demonstrated the vigorous stirring mechanism induced by the spark-induced cavitation. But is this process capable of distorting the fluid stream, namely stretching and folding the fluid, enough to induce

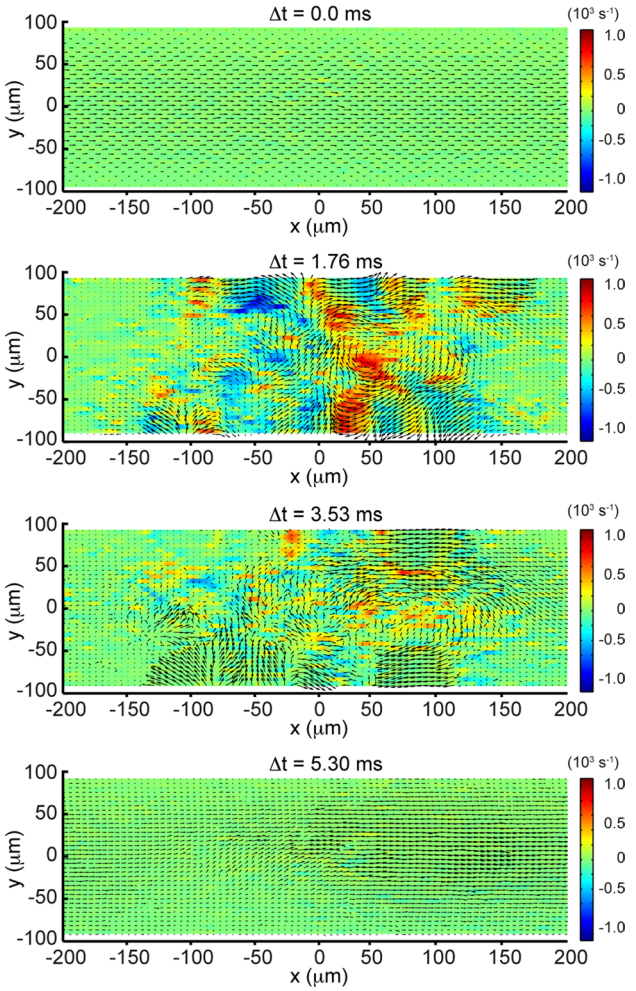

Fig. 4 Microparticle image velocimetry. Time evolution of the velocity field (*arrows*) and vorticity (surface) before and after bubble collapse. The flow is from *left* to *right*, and the coordinate $X = 0$ denotes the position of the tip electrodes

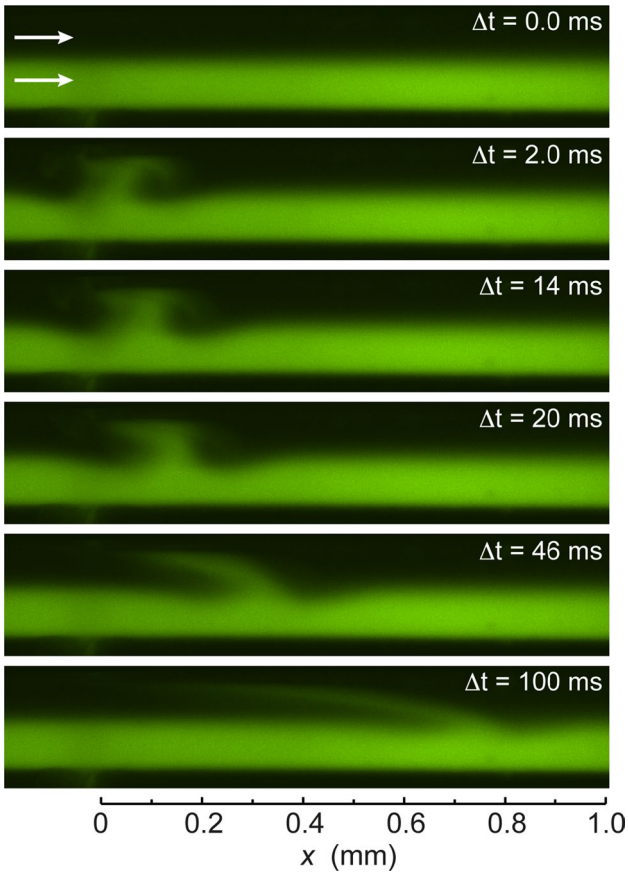

Fig. 5 Fluorescence images acquired at different time instances after the application of a single high-voltage pulse. The flow instability between two adjacent streams (one of them dyed) caused by the collapse of cavitation bubbles is clearly visible. The *two arrows* indicate the flow direction, whereas $X = 0$ denotes the position of the tip electrodes

mixing? To answer this question, we studied the effects of a single high-voltage pulse on two adjacent streams flowing at a mean velocity of ~1.3 mm/s. For visualizing the mixing process, we dyed one of the fluids. A time series of fluorescence micrographs captured with a high-speed camera is shown in Fig. 5. As expected, before the generation of cavitation bubbles ($\Delta t = 0.0$ ms), the two fluids flow side by side without mixing. Interestingly, after bubble collapse ($\Delta t = 2.0$ ms), the interface between the parallel streams becomes unstable, with rotation and distortion of the dyed stream being clearly visible, and a whirl of dyed fluid is formed. As the time progresses, the whirl of dyed fluid gradually turns into a parabolic band ($\Delta t = 46$ ms) that is further stretched along the flow direction by the Taylor dispersion that progressively smears out the dye distribution in the flow direction. At $\Delta t = 100$ ms and onwards, the area containing the mixed fluid flows downstream (i.e., out of the field of view) and the sharp interface between adjacent streams is completely restored. Therefore, the application of a single high-voltage pulse induces the stretching and folding mechanism needed for rapid mixing. It is clear, though, that promoting uniform mixing requires an increase in the frequency of the flow disturbance, that is, operating at a higher pulse repetition rate.

3.4 Micromixing with spark-generated bubbles

We extended the previous study regarding the effects of the cavitation process on the mixing of two adjacent fluids to various spark repetition rates, ranging from 16 to 160 Hz (Fig. 6a). In this case, all images were acquired 180 ms after the application of the external disturbance, with fluids flowing at a mean velocity of 2.7 mm/s. Because we are interested in demonstrating that our approach enables good mixing within small mixing lengths, we focused our analysis on a region of interest (ROI) of 160 μm × 320 μm that

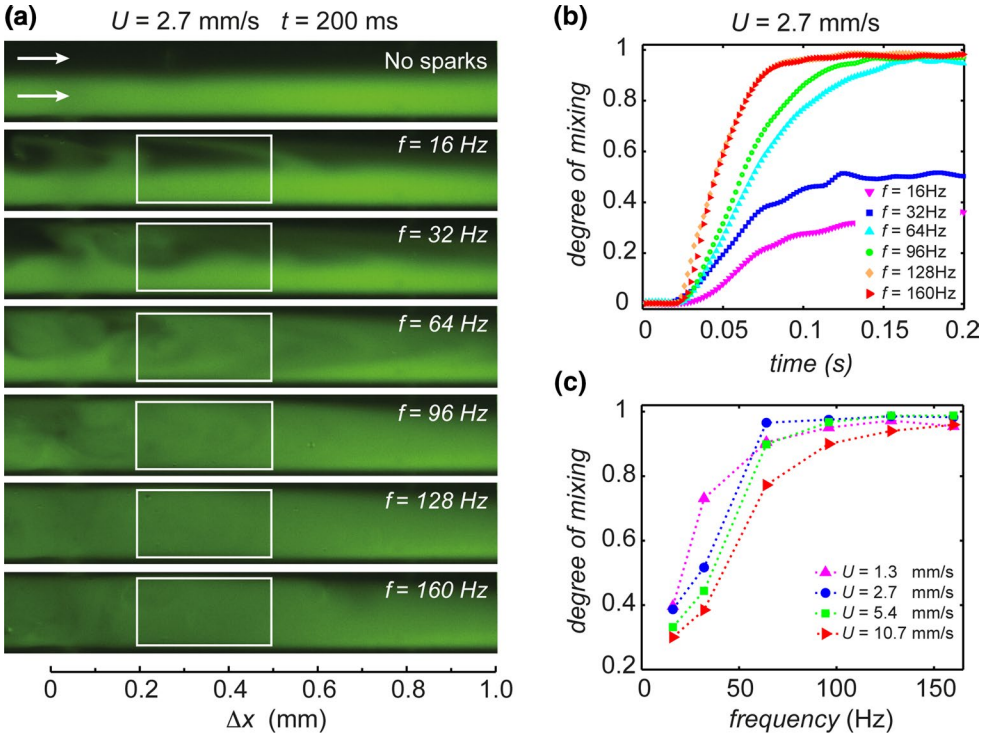

Fig. 6 Quantification of mixing performance. **a** Fluorescence snapshots of the mixing process induced by to the collapse of cavitation bubbles generated using high-voltage pulses at different repetition rates, from 16 to 160 Hz. The *two arrows* indicate the flow direction. The *white frames* denote the ROIs used for the evaluation of the degree of mixing. **b** Plot of the degree of mixing versus time for f ranging from 16 to 160 Hz and $U = 2.7$ mm/s. The initial pulse was applied $t = 20$ ms. **c** Degree of mixing for mean flow velocity from 1.3 to 10.7 mm/s and f from 16 to 160 Hz

we arbitrary located only 200 μm downstream from the tip electrodes (a rectangular frame in Fig. 6a denotes the ROI). Note that at this position, the chaotic flow is already expected to be fully developed (Sundararajan and Stroock 2012). There is a clear trend to increase fluid homogeneity, and hence mixing, as the spark repetition rate increases. Thus, for $f \leq 32$ Hz, the frequency of the disturbance is too low for continuous fluid mixing. In other words, the stirred fluid flows out of the cavitation site before the arrival of a new high-voltage pulse. The presence of parabolic bands of dyed fluid, whose generation is due to a single cavitation event, is in agreement with this observation. As the spark repetition rate increases, the flow exhibits a transition to a time-dependent periodic state (32 Hz $< f <$ 96 Hz) and then to a chaotic steady state ($f \geq 96$ Hz). In particular, for $f \geq 96$ Hz the cumulative effect of multiple cavitation events generates a region of uniform fluorescence intensity within the entire ROI. Note that downstream of the ROI, the mixing is not complete and a clear interface between the dyed and undyed fluids is still visible. This can be explained by considering that 180 ms after the first cavitation event, the homogenized fluid is still transiting trough the ROI and a longer time (~300 ms) is required to uniformly mix the fluids over the entire channel length (~1.3 mm). A movie (Movie 1) in the supplementary material shows the entire dynamics of this mixing process. Therefore, at these conditions, rapid and uniform mixing is achieved only 200 μm downstream from the electrodes. This is a key aspect toward portability and integration in microfluidic devices that contrasts with most existing active mixers that typically require channels at least an order of magnitude longer to achieve satisfactory performance.

A more detailed quantification of the mixing performance of our method in terms of degree of mixing is presented in Fig. 6b, c. In this case, we measured the intensity of fluorescence images such as in Fig. 6a for various fluid flow velocities, ranging from 1.3 to 10.7 mm/s (corresponding flow rates from 5 to 40 μL min). Importantly, an initial calibration showed that the fluorescence intensity is directly proportional to the dye concentration (Fig. S3). Thus, the fluorescence values could be used for measuring the concentration of the dye molecules. To quantify the degree of mixing (Nguyen 2012), we selected as the figure of merit the expression:

$$\eta = 1 - \frac{\sigma}{\sigma_0} \tag{1}$$

where σ and σ_0 correspond, respectively, to the current (after the spark) and reference (before the spark) values of the relative variance of the normalized fluorescence intensity within the ROI, defined as:

$$\sigma = \frac{1}{M \times N} \sum_{i}^{N} \sum_{j}^{M} \frac{\left(I(i,j) - \bar{I}\right)^2}{\bar{I}^2} \tag{2}$$

where $I(i, j)$ is the normalized fluorescence intensity of a pixel with coordinates (i, j), $\bar{I}$ is the reference normalized intensity ($\bar{I} = 0.5$ for a perfect mixing) and $N \times M$

(250 × 500 pixels) is the number of pixel within the ROI. According to our definition of degree of mixing, $\eta = 0$ for unmixed liquids and $\eta = 1$ for completely mixed streams. In the remaining text, in accordance with the existing literature (Sasaki et al. 2006), we consider good mixing as $\eta > 0.90$.

The degree of mixing as function of time for a mean flow velocity of 2.7 mm/s and spark repetition rate from 16 to 160 Hz is presented in Fig. 6b. The values are repeatable, with an uncertainty below 10%. In all instances, η increases over time until reaching a plateau whose value is a function of the repetition rate. Thus, for low spark repetition rates, we found a poor degree of mixing, i.e., $\eta = 0.35$ and $\eta = 0.5$ for $f = 16$ Hz and $f = 32$ Hz, respectively, whereas for higher repetition rates ($f \geq 64$ Hz), an excellent degree of mixing can be achieved, up to a value of 0.98. This confirms the trend observed in Fig. 6a regarding the enhancement of mixing with the frequency of the disturbance. Interestingly, the spark repetition rate not only determines the particular value of attainable η, but it also affects the kinetics of the mixing process. Indeed, the slope of the curves η versus t is higher as the spark repetition rate increases. This can be easily understood by considering that the number of stretch and fold cycles per unit time grows with the spark repetition rate, effectively reducing the diffusion length.

Another relevant parameter that strongly affects the performance of any mixer is the flow velocity. In general, at high flow velocities, i.e., high Péclet number, the mass transport is dominated by advection along the flow direction and mixing becomes more challenging. A plot of the degree of mixing as a function of flow velocity is shown in Fig. 6c. In all cases, and in agreement with Fig. 5a, increasing the spark repetition rate helps to achieve a higher degree of mixing. As expected, the required spark repetition rate to achieve good mixing increases with flow velocity. Importantly, though, our mixer is capable of achieving good mixing over a large span of flow velocities, from $U = 1.3$ mm/s ($Pe = 784$) to $U = 10.7$ mm/s ($Pe = 6274$).

Finally, we analyzed the temporal response of our mixer by measuring the mixing rate or τ_{mix}, defined as the time required to achieve $\eta = 90 \pm 0.02$. By further analyzing the time series of fluorescence images acquired (as in Fig. 6a), we could obtain τ_{mix} for different flow velocities (from 1.3 to 10.7 mm/s) and different spark repetition rates (from 16 to 160 Hz), as shown in Fig. 7. For all the conditions analyzed, τ_{mix} is well below 200 ms. Importantly, by adjusting the spark repetition rate or the flow velocity, it is possible to tune the mixing time down to a value of 42 ms. We can also observe that, for a given flow velocity, the mixing time decreases with the spark repetition rate. This can be easily explained by considering that the increase in the spark repetition rate leads to a larger

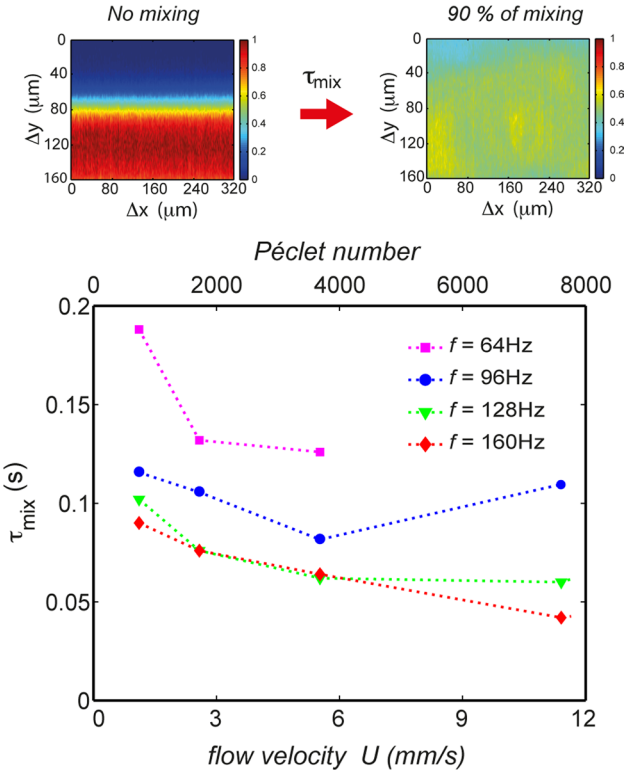

Fig. 7 Evaulation of the mixing dynamics. (*Top*) Schematic representation underlying the definition of the mixing time. (*Bottom*) Plot of the mixing time versus flow velocity for various spark repetition rates. The *top horizontal axis* denotes the Péclet numbers in our experiments, calculated using as the characteristic length the hydraulic diameter of the channel (~245 μm)

number of stretch and fold cycles per unit time and thus a faster mixing. As stated before, there is a minimum number of cycles required to obtain 90% mixing. Otherwise, the fluid never becomes 90% mixed, as it is the case of either $f = 64$ Hz, $U > 5.4$ mm/s or $f < 64$ Hz with any U. More importantly, for a fixed repetition rate, τ_{mix} decreases nonlinearly with increasing the flow velocity. In particular, the mixing time quickly decreases with U in the low-velocity regime (i.e., $U < 3$ mm/s) while it decreases with a lower rate at a higher flow velocity. Also, a degradation of the mixing rate is evident for $f = 96$ Hz and $U = 10.7$ mm/s. This trend is in agreement with the theory of micromixing induced by chaotic advection. Namely, when a steady chaotic flow is developed, the uniform mixing of species with diffusivity D occurs because the diffusion time $\tau_D = \Delta x^2/D$ along the reduced diffusion length $\Delta x \approx \ln(Pe)$ is equal or smaller than the residence time $\tau_{res} = \Delta x/U$ of the stretched and folded fluids. At high Péclet numbers, the condition $\tau_D = \tau_{res}$ leads to the equation $\tau_{mix} = \Delta x/U \approx \ln(Pe)/U = \ln(Pe)/Pe$ (Stroock et al. 2002), and hence τ_{mix} decreases with the flow velocity (i.e., Pe), as experimentally observed. Notably, because this

theory only applies for steady chaotic flows, it is expected that away from these conditions, this dependency of τ_{mix} is not valid, as observed for $f = 96$ Hz, $U = 10.7$ mm/s. In any case, the possibility to tune τ_{mix} by adjusting spark repetition rate or flow rate demonstrated by our mixer provides an additional degree of freedom in terms of controlling chemical reactions according to tailored applications.

4 Conclusions

Spark-generated cavitation bubbles can be used to induce micromixing with high temporal and spatial control. The vigorous stirring mechanism induced by the bubble collapse causes high transverse velocities and vorticities up to 10^3 s^{-1} that can be easily tuned by adjusting the system parameters, namely flow rate and spark repetition rate. As our results demonstrate, excellent mixing over a small length scale of only 200 μm and at high throughput (up to 40 μL/min) can be achieved by using a low-cost and portable electric circuit. Because cavitation enables many other microfluidic functionalities such as micropumping or sorting, our pocket-size solution opens the door for the realization of next-generation portable microfluidics devices where fluid actuation is realized using spark-induced cavitation.

Acknowledgements The authors thank IIT and Compagnia di San Paolo SIME 2015-0682 for financial support. Microscopy data and images for this study were acquired at NIC@IIT (Nikon Imaging Center) at Istituto Italiano di Tecnologia, Genova, Italy.

References

Ahmed D, Mao X, Juluri BK, Huang TJ (2009) A fast microfluidic mixer based on acoustically driven sidewall-trapped microbubbles. Microfluid Nanofluidics 7:727–731

Ballard M, Owen D, Mills ZG et al (2016) Orbiting magnetic microbeads enable rapid microfluidic mixing. Microfluid Nanofluidics 20:88

Brennen CE (1995) Cavitation and bubble dynamics. Oxford University Press, New York

Bruggeman P, Ribežl E, Maslani A et al (2009) Non-thermal plasmas in and in contact with liquids. J Phys D Appl Phys 42:053001/1-28

Buchegger W, Wagner C, Lendl B et al (2011) A highly uniform lamination micromixer with wedge shaped inlet channels for time resolved infrared spectroscopy. Microfluid Nanofluidics 10:889–897

Chan KLA, Niu X, de Mello AJ, Kazarian SG (2010) Rapid prototyping of microfluidic devices for integrating with FT-IR spectroscopic imaging. Lab Chip 10:2170–2174

Chen CK, Cho CC (2008) Electrokinetically driven flow mixing utilizing chaotic electric fields. Microfluid Nanofluidics 5:785–793

Dijkink R, Ohl C-D (2008) Laser-induced cavitation based micropump. Lab Chip 8:1676–1681

Dittrich PS, Tachikawa K, Manz A (2006) Micro total analysis systems. Latest advancements and trends. Anal Chem 78:3887–3908

Duocastella M, Fernández-Pradas JM, Morenza JL, Serra P (2009) Time-resolved imaging of the laser forward transfer of liquids. J Appl Phys 106:084907

Duocastella M, Florian C, Serra P, Diaspro A (2015) Sub-wavelength laser nanopatterning using droplet lenses. Sci Rep 5:16199

Elvira KS, Casadevall i Solvas X, Wootton RCR, de Mello AJ (2013) The past, present and potential for microfluidic reactor technology in chemical synthesis. Nat Chem 5:905–915

Hai-lang Z, Shi-jun H (1996) Viscosity and density of water + sodium chloride + potassium chloride solutions at 298.15 K. J Chem Eng Data 41:516–520

Hellman AN, Rau KR, Yoon HH et al (2007) Laser-induced mixing in microfluidic channels. Anal Chem 79:4484–4492

Jeong GS, Chung S, Kim C-B, Lee S-H (2010) Applications of micromixing technology. Analyst 135:460–473

Lee CY, Chang CL, Wang YN, Fu LM (2011) Microfluidic mixing: a review. Int J Mol Sci 12:3263–3287

Luong T-D, Phan V-N, Nguyen N-T (2010) High-throughput micromixers based on acoustic streaming induced by surface acoustic wave. Microfluid Nanofluidics 10:1–7

Nguyen N-T (2012) Micromixers: fundamental, design and fabrication, 2nd edn. William, Andrew

Ozcelik A, Ahmed D, Xie Y et al (2014) An acoustofluidic micromixer via bubble inception and cavitation from microchannel sidewalls. Anal Chem 86:5083–5088

Park S-Y, Wu T-H, Chen Y et al (2011) High-speed droplet generation on demand driven by pulse laser-induced cavitation. Lab Chip 11:1010–1012

Qian J, Joshi RP, Schamiloglu E et al (2006) Analysis of polarity effects in the electrical. J Phys D Appl Phys 39:359–369

Qin D, Xia Y, Whitesides GM (2010) Soft lithography for micro- and nanoscale patterning. Nat Protoc 5:491–502

Sasaki N, Kitamori T, Kim H-B (2006) AC electroosmotic micromixer for chemical processing in a microchannel. Lab Chip 6:550–554

Schindelin J, Arganda-Carreras I, Frise E et al (2012) Fiji: an open-source platform for biological-image analysis. Nat Methods 9:676–682

Schönfeld F, Hessel V, Hofmann C (2004) An optimised split-and-recombine micro-mixer with uniform chaotic mixing. Lab Chip 4:65–69

Sigurdson M, Wang D, Meinhart CD (2005) Electrothermal stirring for heterogeneous immunoassays. Lab Chip 5:1366–1373

Singh AK, Ko D-H, Vishwakarma NK et al (2016) Micro-total envelope system with silicon nanowire separator for safe carcinogenic chemistry. Nat Commun 7:10741

Song H, Cai Z, Noh HM, Bennett DJ (2010) Chaotic mixing in microchannels via low frequency switching transverse electroosmotic flow generated on integrated microelectrodes. Lab Chip 10:734–740

Stroock AD, Dertinger SKW, Ajdari A et al (2002) Chaotic mixer for microchannels. Science 295:647–651

Suh YK, Kang S (2010) A review on mixing in microfluidics. Micromachines 1:82–111

Sundararajan P, Stroock AD (2012) Transport phenomena in chaotic laminar flows. Annu Rev Chem Biomol Eng 3:473–496

Therriault D, White SR, Lewis JA (2003) Chaotic mixing in three-dimensional microvascular networks fabricated by direct-write assembly. Nat Mater 2:265–271

Wen CY, Yeh CP, Tsai CH, Fu LM (2009) Rapid magnetic microfluidic mixer utilizing AC electromagnetic field. Electrophoresis 30:4179–4186

Yaralioglu GG, Wygant IO, Marentis TC, Khuri-Yakub BT (2004) Ultrasonic mixing in microfluidic channels using integrated transducers. Anal Chem 76:3694–3698

Zwaan E, Le Gac S, Tsuji K, Ohl CD (2007) Controlled cavitation in microfluidic systems. Phys Rev Lett 98:22–25